Title

Visible spatial frequency domain imaging with a digital light microprojector

Journal

Journal of Biomedical Optics, 18(9)

ISSN

1083-3668

Authors

Lin, Alexander J

Ponticorvo, Adrien

Konecky, Soren D

et al.

Publication Date

2013-09-04

DOI

10.1117/1.jbo.18.9.096007

Peer reviewed

Journal of Biomedical Optics

SPIEDigitalLibrary.org/jbo

Visible spatial frequency domain imaging with a digital light microprojector

Alexander J. Lin
Adrien Ponticorvo
Soren D. Konecky
Haotian Cui
Tyler B. Rice
Bernard Choi
Anthony J. Durkin
Bruce J. Tromberg

SPIE

Visible spatial frequency domain imaging with a digital light microprojector

Alexander J. Lin,[a,b] Adrien Ponticorvo,[a] Soren D. Konecky,[a] Haotian Cui,[a,b] Tyler B. Rice,[a] Bernard Choi,[a,b,c] Anthony J. Durkin,[a] and Bruce J. Tromberg[a,b]
[a]University of California, Beckman Laser Institute and Medical Clinic, Department of Surgery, Irvine, California
[b]University of California, Department of Biomedical Engineering, Irvine, California
[c]University of California, Edwards Lifesciences Center for Advanced Cardiovascular Technology, Irvine, California

Abstract. There is a need for cost effective, quantitative tissue spectroscopy and imaging systems in clinical diagnostics and pre-clinical biomedical research. A platform that utilizes a commercially available light-emitting diode (LED) based projector, cameras, and scaled Monte Carlo model for calculating tissue optical properties is presented. These components are put together to perform spatial frequency domain imaging (SFDI), a model-based reflectance technique that measures and maps absorption coefficients (μ_a) and reduced scattering coefficients (μ_s') in thick tissue such as skin or brain. We validate the performance of the flexible LED and modulation element (FLaME) system at 460, 530, and 632 nm across a range of physiologically relevant μ_a values (0.07 to 1.5 mm^{-1}) in tissue-simulating intralipid phantoms, showing an overall accuracy within 11% of spectrophotometer values for μ_a and 3% for μ_s'. Comparison of oxy- and total hemoglobin fits between the FLaME system and a spectrophotometer (450 to 1000 nm) is differed by 3%. Finally, we acquire optical property maps of a mouse brain *in vivo* with and without an overlying saline well. These results demonstrate the potential of FLaME to perform tissue optical property mapping in visible spectral regions and highlight how the optical clearing effect of saline is correlated to a decrease in μ_s' of the skull. [DOI: 10.1117/1.JBO.18.9.096007]

Keywords: tissue optics; spatial frequency domain imaging; microprojector; scattering; absorption; neuroimaging.

Paper 130222R received Apr. 9, 2013; revised manuscript received Jul. 16, 2013; accepted for publication Jul. 31, 2013; published online Sep. 4, 2013.

1 Introduction

Spatial frequency domain imaging (SFDI) is a reflectance-based technique that can measure and map absorption (μ_a) and scattering (μ_s') coefficients in tissue on a pixel-by-pixel basis. SFDI works by structuring light into sinusoidal patterns and projecting them onto the tissue surface. The tissue acts as a spatial filter and blurs the structured patterns. By projecting patterns of differing spatial frequencies, the modulation transfer function of the tissue can be found from which a unique pair of optical absorption and scattering coefficients is determined. Further filtering of the remitted light with either a series of bandpass filters or with a liquid-crystal tunable filter allows unique spectra of μ_a and μ_s' to be found in different tissue types.[1,2]

Recent applications of SFDI to skin imaging include *in vivo* monitoring of burn wounds,[3,4] determining flap perfusion during surgical procedures,[5,6] and assessing cutaneous vascular abnormalities.[7] SFDI has also been used for characterizing brain in small animal models of stroke,[8] glioblastoma,[9] and Alzheimer's disease.[10] In each example, multispectral maps of tissue scattering are separately constructed from tissue absorption. This allows formation of chromophore images such as oxyhemoglobin (HbO_2), deoxy-hemoglobin (Hb), lipid, and water using the Beer–Lambert law. The inverse relationship between spatial frequency and average photon pathlength[11] also facilitates SFDI depth sectioning and tomography of absorbing and fluorescent inhomogeneities.[12–14]

In this work, we present a low cost, three-wavelength SFDI system that operates in the visible spectral regime using three light-emitting diodes (LEDs) (460, 530, and 632 nm). The cost savings of a consumer electronics-based SFDI system can be appreciated by comparing the price of a commercial LED microprojector (e.g., ~250 for an AAXA M2 microprojector) with that of a scientific-grade digital light projector (e.g., ~8000 for a Texas Instrument DLP Discovery 4100 Kit). We sought to quantify this consumer-grade SFDI system's performance in the more challenging visible regime where $\mu_a \sim \mu_s'$ and small amounts of noise in measured light levels can introduce large inaccuracies in separating absorption from scattering.[2] SFDI instrumentation is described and validated in tissue-simulating Intralipid phantoms, and optical property maps of a mouse brain are measured in order to demonstrate overall sensitivity and performance. In addition, we examine the impact of saline windows commonly used in rodent model neuroimaging in order to assess how this preparation may influence tissue absorption and scattering values. Implementation of our system offers great potential for measuring optical properties of superficial tissues such as skin epidermis and rodent brain cortex.

2 Methods

2.1 *Flexible LED and Modulation Element (FLaME) Instrumentation*

We modified a LED-based microprojector (M2, AAXA Technologies, Inc., Tustin, California) to project a field of view of 40×30 mm^2 by extending the focusing tube lens slightly beyond the manufactured limit. All other settings and

Address all correspondence to: Bruce J. Tromberg, Beckman Laser Institute, 1002 Health Sciences Road, Irvine, California 92612. Tel: +949-824-8705; Fax: +949-824-8413; E-mail: bjtrombe@uci.edu

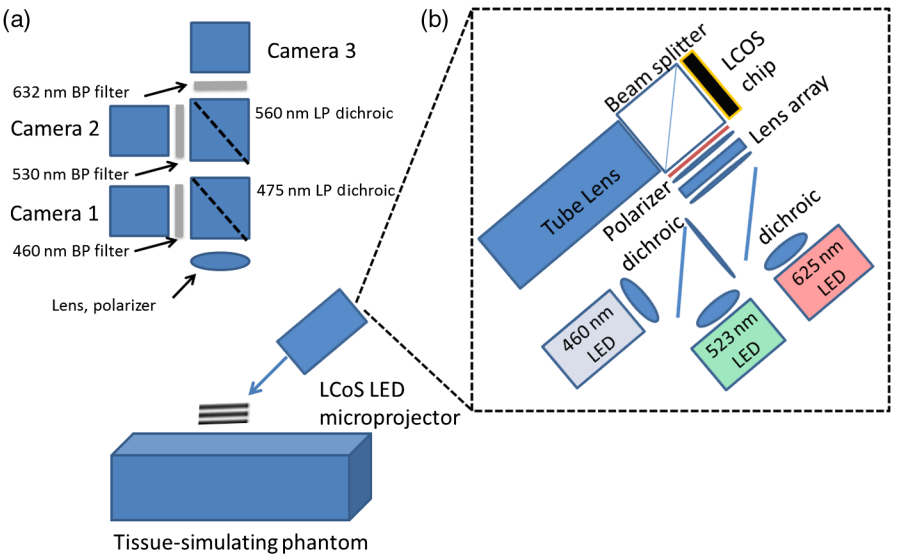

Fig. 1 (a) Diagram of FLaME experimental imaging setup. All components were controlled using LabVIEW software on a personal computer. (b) Expanded view of the AAXA M2 microprojector.

components of the projector were used as received, including the three individual blue, green, and red LEDs centered at 460, 523, and 625 nm, respectively [Fig. 1(b)]. These wavelengths are sufficient for differentiating oxy- and deoxy-hemoglobin concentration: 523 nm is near an isosbestic point for oxy- and deoxy-hemoglobin, oxy-hemoglobin is about twice as absorbing as deoxy-hemoglobin at 460 nm, and deoxy-hemoglobin is about four times as absorbing as oxy-hemoglobin at 625 nm [Fig. 3(a)]. The projector was used as a second monitor and images were created in Matlab (Mathworks) and displayed as figures in the second monitor. The refresh rate of the liquid crystal on silicon chip in the AAXA projector was 70 Hz or about 14.286 ms/frame. Thus, we used multiples of 14.286 ms as the exposure time to achieve consistent light levels.

As shown in the block diagram in Fig. 1(a), multispectral reflectance images were separated spectrally with dichroic mirrors (475DCLP, 560DCLP, Omega Optical, Inc., Brattleboro, Vermont) and bandpass filters (FB460-10, FB530-10, FL632.8-10, Thorlabs, Inc., Newton, New Jersey). Filtered images were detected using three 12-bit charge-coupled device cameras (Flea2G, Point Grey, Richmond, BC, Canada). Images from the three cameras were co-registered with one another using a fiducial marker (reflective sticker, 1-mm diameter) on

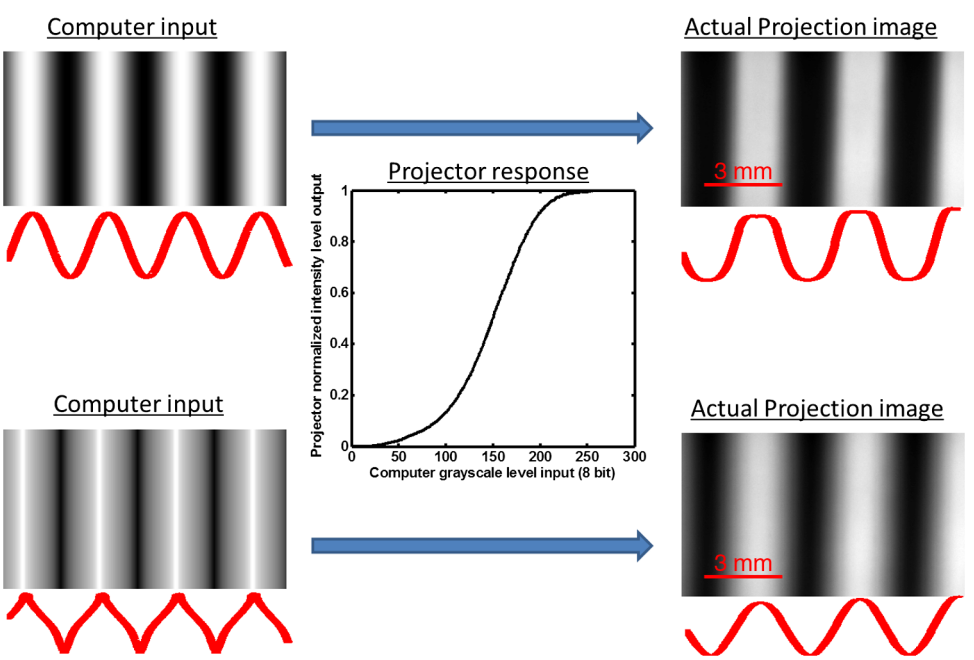

Fig. 2 The nonlinear input–output intensity curve (gamma function) of the projector (middle) distorts a sine wave image input from the computer (top left) to appear as a square wave (top right). Using the projector response function as a look-up-table, the computer image input was adjusted such that the actual projected image (bottom left) is sinusoidal when detected on spectralon (Labsphere) (bottom right). Cross-section intensity profiles of the images are shown in red under the images to better illustrate the projection transformation.

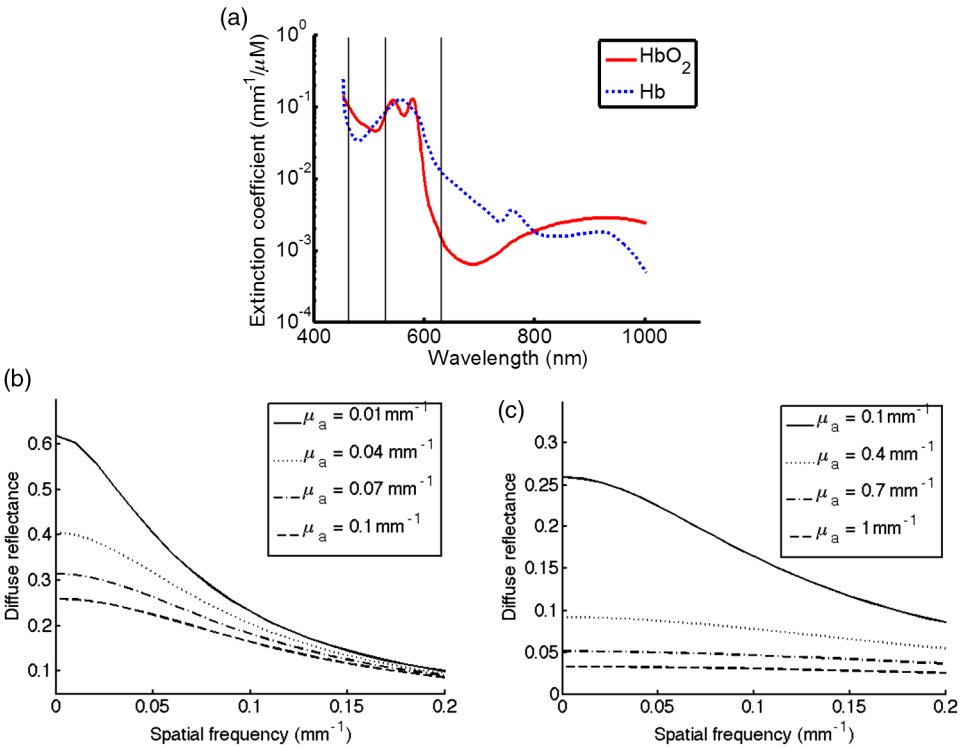

Fig. 3 (a) Absorption spectra of oxy-hemoglobin (HbO_2) and deoxy-hemoglobin (Hb). Vertical lines highlight 460, 530, and 632 nm absorption features. (b) Scaled Monte Carlo predictions of diffuse reflectance as a function of spatial frequency with μ_s' constant at 1 mm^{-1} and μ_a increasing by increments of 0.03 mm^{-1} from 0.01 to 0.1 mm^{-1}. (c) Scaled Monte Carlo predictions of diffuse reflectance as a function of spatial frequency with μ_s' constant at 1 mm^{-1} and μ_a increasing by increments of 0.3 mm^{-1} from 0.1 to 1 mm^{-1}.

a solid tissue-simulating phantom.[15] A crossed linear polarizer (Edmund Optics, Barrington, New Jersey) was also placed before the cameras to reduce the effect of specular reflectance from the sample. The input–output curve (gamma function) of the projector was determined empirically by sequentially projecting 256 grayscale level images on spectralon (Labsphere) and recording the average pixel intensity from the camera, normalized to the brightest projection (Fig. 2). We found that the nonlinear gamma function of the projector distorts a sine wave image input from the computer to appear as a square wave. We adjusted the computer image input levels, based on the gamma function, such that the actual projected image was sinusoidal when detected (Fig. 2). The projector and cameras were connected to a personal computer and controlled by custom LabVIEW software (National Instruments, Austin, Texas).

2.2 *SFDI in the Visible*

Optical properties were calculated using a multifrequency fitting approach described previously.[1] We sequentially projected five spatial frequencies (0, 0.05, 0.1, 0.2, and 0.4 mm^{-1}) with each sinusoidal frequency pattern projected three times at phases of 0, 120, and 240 deg. The remitted reflectance was captured by the three cameras simultaneously and saved for offline processing and analysis. Acquisition speed was limited by the camera exposure times for highly absorbing samples (~300 ms for 460 and 530 nm) and software synchronization of the projector display with camera frame grab (this added ~800 ms/frame grab). Total acquisition time for 10 repetitions of five spatial frequencies at three phases (150 images) was approximately 3 min or ~1.1 s/frame. More rapid tissue imaging could be achieved by improving light collection optics and camera sensitivity as well as using dedicated acquisition and control software. Reflectance at each spatial frequency and wavelength was calculated using

$$R_{fx} = (2^{1/2}/3) \times [(I_1 - I_2)^2 + (I_1 - I_3)^2 + (I_2 - I_3)^2]^{1/2}, \quad (1)$$

where R_{fx} is the demodulated frequency amplitude image and I_1, I_2, and I_3 are the three captured images at the three different phases by each camera. R_{fx} images were further calibrated to silicone phantoms of known optical properties to correct for any system error such as light inhomogeneity or lens aberration. The optical properties of the reference phantoms were acquired using spatially modulated quantitative spectroscopy.[16] The frequency-dependent diffuse reflectance (R_d) was then fit to a Monte Carlo model of light transport,[2] and absorption (μ_a) and reduced scattering (μ_s') coefficients were calculated on a pixel-by-pixel basis. All analyses were done in Matlab (MathWorks, Natick, Massachusetts).

2.3 *Phantom Validations*

Hemoglobin is approximately an order of magnitude more absorbing in the blue–green wavelengths (e.g., 460 and 530 nm) versus 632 nm and above[17] [Fig. 3(a)]. While SFDI has been validated in the near-infrared (NIR)[2] where $\mu_a \ll \mu_s'$, we needed to establish that FLaME could be used to separate absorption from scattering when $\mu_a \sim \mu_s'$. To determine the relevant range of μ_a values, we used the Beer–Lambert law to predict μ_a at the three wavelengths when total hemoglobin (THb) ranged from 50 to 150 μM with 60% oxygen saturation (μ_a = 0.03 to 1.3 mm^{-1}). Our previous work in mice showed a

THb around 150 μM[10] while others have used concentrations of around 100 μM.[18] Then, keeping μ_s' constant at 1 mm^{-1}, we used a scaled Monte Carlo model[2] to predict reflectance as a function of spatial frequency when we varied μ_a from 0.01 to 0.1 mm^{-1} [Fig. 3(b)] and from 0.1 to 1 mm^{-1} [Fig. 3(c)]. The reflectance changes much more with respect to spatial frequency ($\delta R_d/\delta fx$) in the lowest absorbing sample ($\delta R_d/\delta fx = 2.6$ mm) versus the highest absorbing sample ($\delta R_d/\delta fx = 0.038$ mm), showing low signal-to-noise may be a source of error when inverting the model and fitting for μ_a and μ_s' at high values of μ_a.

To validate the performance of the system, we conducted a series of controlled experiments in tissue-simulating phantoms. First, 19 mL solutions of 0.25, 0.5, and 1 g/L napthol green B solution (Sigma, St. Louis, Missouri) were made in double-distilled water and measured in transmission mode with a VIS–NIR spectrophotometer (UV-3600, Shimadzu, Inc., Kyoto, Japan) from 450 to 1000 nm. Similarly, a sample of fresh pig blood was acquired (protocol No. 2007-2743), stored in a vial with heparin anticoagulant, and diluted to a 1:100 ratio in phosphate-buffered saline before being measured in the spectrophotometer. The μ_a absorption spectra were calculated by taking the negative logarithm of the percent transmission and dividing by the pathlength traveled (10 mm for the dye solutions, 5 mm for the pig blood solution). After measurement with the spectrophotometer, 1 mL of 20% Intralipid (Fresenius Kabi, Bad Homburg, Germany) was then added to 19 mL of the solutions to mimic scattering in tissue[19] and each solution was measured with the FLaME system.

2.4 *In Vivo Mouse Brain*

We imaged a 3-month-old C57BL/6 mouse under 1.2% isoflurane anesthesia in a 21% oxygen/79% nitrogen air mix (Oxydial, Starr Life Sciences Corp., Oakmont, Pennsylvania). After inducing anesthesia (2% isoflurane), the head was secured in a stereotaxic frame (Stoelting Co., Wood Dale, Illinois) and

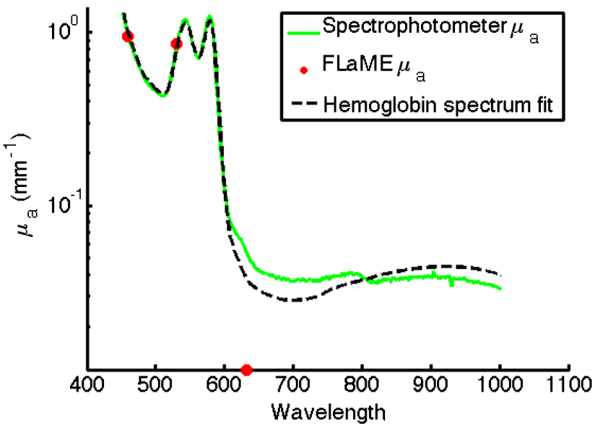

Fig. 5 Blood phantom spectra acquired using a conventional transmission spectrophotometer (thick green line), FLaME (red dots), and the best fit of the spectrophotometer data to hemoglobin (dashed black line). Standard deviations for FLaME data are $\sigma_{460\,nm} = 0.05$ mm^{-1}, $\sigma_{530\,nm} = 0.04$ mm^{-1}, and $\sigma_{632\,nm} = 0.002$ mm^{-1}. They are not shown for clarity.

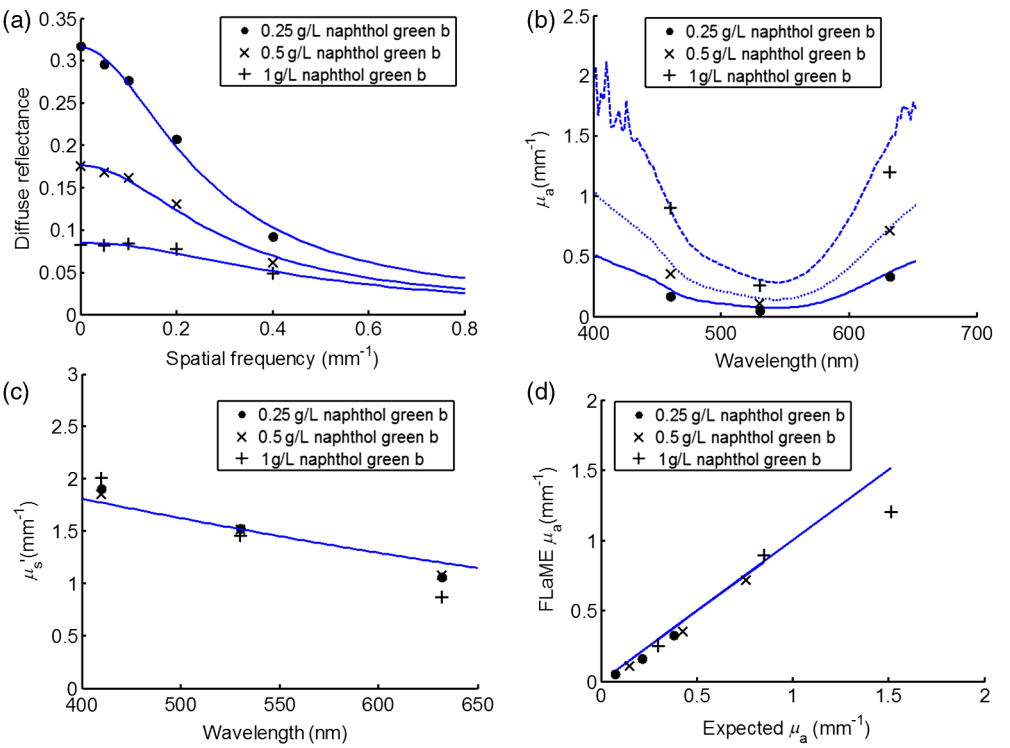

Fig. 4 (a) Example plot of R_d at 0, 0.05, 0.1, 0.2, and 0.4 mm^{-1} spatial frequencies for three concentrations of napthol green B at 460 nm. Lines are the least-squares fits of the Monte Carlo forward model of R_d as a function of μ_a and μ_s'. Standard deviation bars of the data <0.006 and are not shown for clarity. (b) Plot of μ_a spectra of three concentrations of napthol green B. Lines are from the spectrophotometer and points are from FLaME measurements. Standard deviation bars of the FLaME data <0.03 and are not shown for clarity. (c) Plot of μ_s' spectra of three concentrations of napthol green B in 1% Intralipid solution. Line is the expected scattering of 1% Intralipid from Mie theory. Standard deviation bars of the FLaME data <0.07 and are not shown for clarity. (d) Plot of data from (b) showing an outlier in FLaME data when the expected $\mu_a = 1.5$ mm^{-1}.

Table 1 Table of oxy-hemoglobin (HbO_2) and deoxy-hemoglobin (Hb) fits determined from the spectrophotometer spectrum (450 to 1000 nm) and from the FLaME absorption data at 460, 530, and 632 nm.

	HbO_2 (μM)	Hb (μM)
Spectrophotometer (450 to 1000 nm)	87.7	3.0
FLaME (460/530/632 nm)	90.4 ± 6.3	3.6 ± 5.2

Table 2 Absorption and reduced scattering coefficients acquired from FLaME imaging of the blood/Intralipid phantom are shown with standard deviation of the 150,880 pixels in the regions of interest.

FLAME	460 nm	530 nm	632 nm
μ_a (mm^{-1})	0.95 ± 0.05	0.86 ± 0.04	0.011 ± 0.002
μ_s' (mm^{-1})	2.18 ± 0.11	1.63 ± 0.07	1.32 ± 0.03

body temperature was maintained at 37°C with a thermocouple-controlled heating pad (Cwe, Inc., Ardmore, Pennsylvania). We removed the skin and fascia above the scalp and a well was created with petroleum jelly around the regions of interest (ROI), filled with sterile saline, and covered with a glass coverslip to maintain optical transparency of the skull. A similar well was created on the calibration phantom during FLaME measurements. For determining the effect of the saline well, we prepared a 2-month old senescence-accelerated mouse-prone 8 transgenic mouse as above, but imaged it both with and without the saline well. All procedures were performed in accordance with the regulations of the Institutional Animal Care and Use Committee (IACUC) of the University of California, Irvine (protocol 2010-2934).

3 Data Analysis

In post-processing, the 10 repetitions of raw images acquired were averaged before being demodulated, calibrated, and fitted for μ_a and μ_s'. Values for μ_a, μ_s', and hemoglobin were calculated for each pixel in the image. THb was calculated as the sum of oxy-hemoglobin (HbO_2) and deoxy-hemoglobin (Hb). Oxygen saturation (O_2 sat) was calculated as $(HbO_2/THb) \times 100$. ROI were selected and an average value with standard deviation was calculated for each ROI. For phantom comparisons with the spectrophotometer, FLaME-derived μ_a was multiplied by 1.05 to account for dilution with 1 mL Intralipid in 19 mL solution. All analyses were done in MATLAB.

4 Results and Discussion

The strategy to use multiple spatial frequencies in fitting for μ_a and μ_s' was integral in minimizing fitting error, as the impact of uncertainties in diffuse reflectance measurements at one spatial frequency is reduced and data fits are better constrained by multifrequency content [Fig. 4(a)]. The fitted absorption coefficients in the napthol green B titrations were on average -0.064 ± 0.095 mm^{-1} different from spectrophotometer μ_a's, or $-16\% \pm 11\%$ off [Fig. 4(b)]. If the data are plotted as FLaME μ_a versus spectrophotometer μ_a [Fig. 4(d)], it is more apparent at $\mu_a = 1.5$ mm^{-1} that the FLaME fit is an outlier. Without this highest point, the FLaME μ_a's were on average -0.035 ± 0.034 mm^{-1} different from spectrophotometer μ_a's, or $-11\% \pm 13\%$ off. While there is a natural variation in Intralipid batches,[20] we show in Fig. 4(c) that FLaME-fitted scattering values are within the range of the Mie theory-predicted scattering for 1% Intralipid,[21] with a mean error of $3\% \pm 0.3\%$.

Interestingly, the -0.035 mm^{-1} offset in the FLaME-fitted μ_a's compared to the spectrophotometer artificially causes a higher percentage of error at the lower μ_a's (~30%) compared to the higher μ_a's (~5%). Better calibration of the silicone reference phantom at visible wavelengths is needed to correct for this offset.

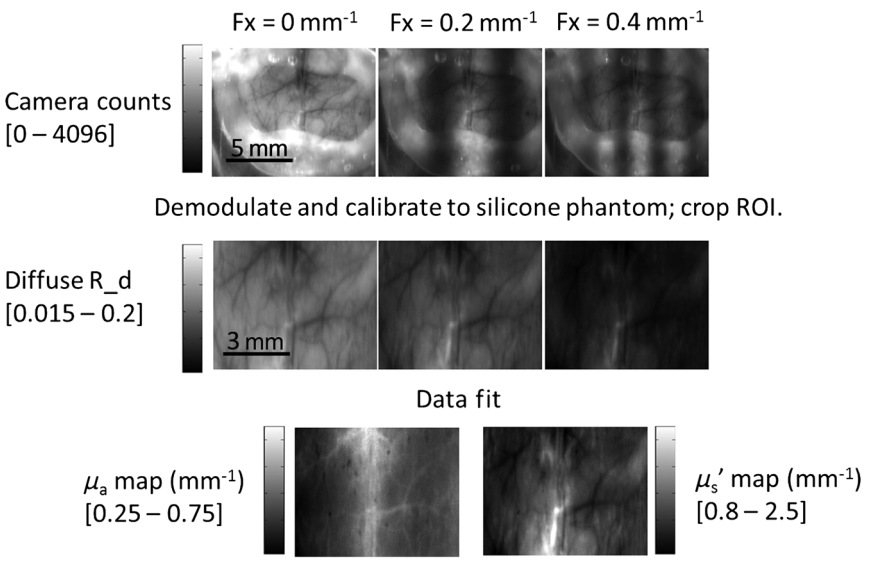

Fig. 6 A summary of the SFDI process in a mouse brain at 530 nm: (Top row) Raw camera snapshots of mouse brain with projected spatial frequencies. (Middle row) Cropped and calibrated diffuse reflectance images of the mouse brain as a function of spatial frequency. (Bottom row) Pixel-by-pixel fitted μ_a and μ_s' maps of the mouse brain at 530 nm. The midsagittal vein, a prominent vessel on the midline surface of the brain, can be seen on the μ_a map. The sagittal skull suture is marked by increased scattering on the μ_s' map.

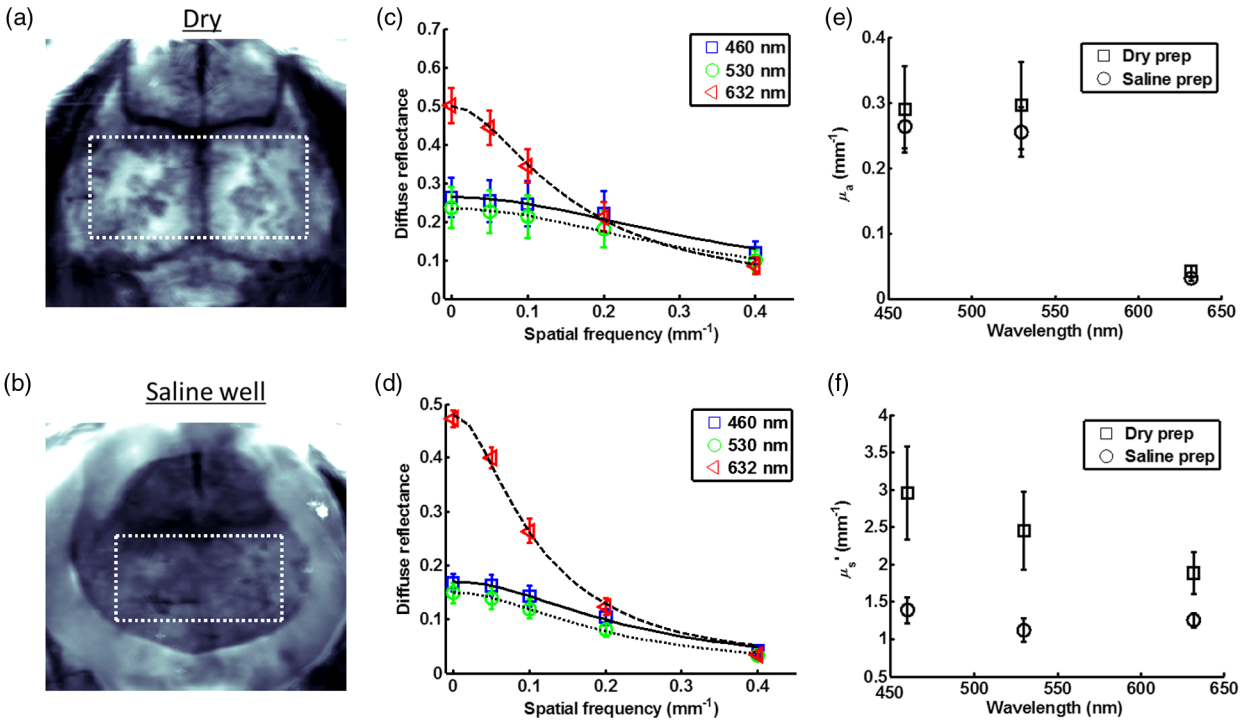

Fig. 7 Adding a saline well over the skull, as commonly done in optical intrinsic signal imaging causes a significant ($p < 0.05$) decrease in the detected scattering when compared to imaging a dry skull. (a and b) Images of the dry and saline-soaked regions of interest (ROI). Plots of diffuse reflectance as a function of spatial frequency for the dry skull (c) and the wet skull (d). (e) A comparison of fitted μ_a values for a dry skull (squares) versus a wet skull (circles). (f) A comparison of fitted μ_s' values for a dry skull (squares) versus a wet skull (circles). All error bars are standard deviation of the ROI pixels.

In Fig. 5, we see FLaME μ_a values within 7% of spectrophotometer values for 460 and 530 nm, but the much lower absorption of blood at 632 nm results in a 78% error (0.011 mm^{-1} versus 0.051 mm^{-1}). Absorption measurements at the three wavelengths were fit to hemoglobin concentrations using the Beer–Lambert law and compared to hemoglobin fits from the spectrophotometer (Table 1). For the spectrophotometer measurement, scattering of the red blood cells was modeled to follow a wavelength-dependent power law, $\mu_s' = A\lambda^{-b}$,[22] where A is the scattering amplitude and b is the scattering power. Previously, Mourant et al. showed microspheres with diameters of 0.1 to 2 μm in solution have b value magnitudes ranging from 4 to 0.37, respectively.[22] The diameter of red blood cells in pig blood is 6 μm,[23] so we assumed b to be 0.37 and scattering amplitude, A, was fit for as the third chromophore in the Beer–Lambert law and found to be 1.4×10^6. FLaME comparisons with the spectrophotometer hemoglobin fits were within 3% for HbO_2, 20% for Hb, 4% for Total Hb, and O_2 saturation was 96.7% (spectrophotometer) versus 96.2% (FLaME) (Table 1). The fitted μ_s' values from FLaME (Table 2) were slightly higher than the napthol green B measurements, probably from the additional scattering from the red blood cells.

A potential application of the FLaME system is to characterize rodent brain absorption and scattering properties in disease models, assess physiologic changes, and monitor therapeutic interventions. We show below in Fig. 6, the mouse brain with skull intact being imaged with 530 nm light. As expected, vessels are clearly seen in the raw and diffuse reflectance images from THb absorption as well as in the μ_a and μ_s' maps.

While we used saline to reduce specular reflections from a dry skull, it is unknown how this might affect the detected optical properties. In Fig. 7, we show the FLaME system is sensitive to a reduction in μ_s' when saline is added to the skull [Fig. 7(f)]. As expected, the scatter-corrected absorption [Fig. 7(e)] and hemoglobin concentrations (Table 3) do not differ significantly. Visible wavelengths only penetrate 250 to 500 μm into tissue,[24] and optical properties of overlying rodent skull can significantly contribute to optical properties measured by SFDI. The ability to measure intrinsic tissue scattering and the impact of saline well or similar preparations can improve measurement accuracy and allow more quantitative comparisons between different subjects.

Table 3 Fitted hemoglobin concentrations and oxygen saturation for FLaME imaging of a brain with an overlying dry skull versus saline-soaked skull.

	HbO_2 (μM)	Hb (μM)	THb (μM)	O_2 sat (%)
Dry prep	19 ± 7	16 ± 8	35 ± 8	55 ± 17
Saline prep	20 ± 3	11 ± 4	31 ± 4	64 ± 9

5 Conclusion

We have described a low-cost multispectral imaging platform that uses a commercially available LED-based digital light projector and a scaled Monte Carlo light propagation model to acquire tissue absorption and reduced scattering properties in visible (blue, green, and red) spectral regions using SFDI. No modifications to the microprojector hardware is required, however, computer-synthesized projection patterns must be corrected for nonuniformities in projector output using a calibration procedure. The accuracy of the FLaME system was 11% and 3%, respectively, for determining μ_a and μ_s' in tissue-simulating

liquid phantoms over a ~20-fold range of realistic tissue absorption values. FLaME measurements of oxy-, deoxy-hemoglobin, and THb were within 3% to 20% of true values as determined by a spectrophotometer. Optical absorption and scattering maps of a mouse brain were measured *in vivo* with visible light for the first time, showing this easily accessible platform may have applications in multispectral neuroimaging and similar settings that require quantitative assessment of tissue hemodynamics and composition.

Acknowledgments

Funding for this work was supported by the NIH (NIBIB) Laser Microbeam and Medical Program (P41EB015890), NIH (NIA) Grant (R01 A6-21982), NIH (NIA) Ruth Kirschstein NRSA fellowship (5F30AG039949-02), NIH (NIBIB) Grant (R21 EB014440), NIH (NINDS) Grant (R21 NS078634), UC Irvine MSTP, and the Arnold and Mabel Beckman Foundation. The authors would also like to thank Kendrew Au, M.S., for his help in calibrating reference phantoms.

References

1. D. J. Cuccia et al., "Modulated imaging: quantitative analysis and tomography of turbid media in the spatial-frequency domain," *Opt. Lett.* **30**(11), 1354–1356 (2005).
2. D. J. Cuccia et al., "Quantitation and mapping of tissue optical properties using modulated imaging," *J. Biomed. Opt.* **14**(2), 024012 (2009).
3. M. Kaiser et al., "Noninvasive assessment of burn wound severity using optical technology: a review of current and future modalities," *Burns* **37**(3), 377–386 (2011).
4. T. T. Nguyen et al., "Novel application of a spatial frequency domain imaging system to determine signature spectral differences between infected and noninfected burn wounds," *J. Burn Care Res.* **34**(1), 44–50 (2013).
5. A. Yafi et al., "Postoperative quantitative assessment of reconstructive tissue status in a cutaneous flap model using spatial frequency domain imaging," *Plast. Reconstr. Surg.* **127**(1), 117–130 (2011).
6. S. Gioux et al., "First-in-human pilot study of a spatial frequency domain oxygenation imaging system," *J. Biomed. Opt.* **16**(8), 086015 (2011).
7. A. Mazhar et al., "Spatial frequency domain imaging of port wine stain biochemical composition in response to laser therapy: a pilot study," *Lasers Surg. Med.* **44**(8), 611–621 (2012).
8. D. Abookasis et al., "Imaging cortical absorption, scattering, and hemodynamic response during ischemic stroke using spatially modulated near-infrared illumination," *J. Biomed. Opt.* **14**(2), 024033 (2009).
9. S. D. Konecky et al., "Spatial frequency domain tomography of protoporphyrin IX fluorescence in preclinical glioma models," *J. Biomed. Opt.* **17**(5), 056008 (2012).
10. A. J. Lin et al., "Spatial frequency domain imaging of intrinsic optical property contrast in a mouse model of Alzheimer's disease," *Ann. Biomed. Eng.* **39**(4), 1349–1357 (2011).
11. T. D. O'Sullivan et al., "Diffuse optical imaging using spatially and temporally modulated light," *J. Biomed. Opt.* **17**(7), 071311 (2012).
12. S. D. Konecky et al., "Quantitative optical tomography of sub-surface heterogeneities using spatially modulated structured light," *Opt. Express* **17**(17), 14780–14790 (2009).
13. A. Mazhar et al., "Structured illumination enhances resolution and contrast in thick tissue fluorescence imaging," *J. Biomed. Opt.* **15**(1), 010506 (2010).
14. C. D'Andrea et al., "Fast 3D optical reconstruction in turbid media using spatially modulated light," *Biomed. Opt. Express* **1**(2), 471–481 (2010).
15. J. Q. Nguyen et al., "Effects of motion on optical properties in the spatial frequency domain," *J. Biomed. Opt.* **16**(12), 126009 (2011).
16. R. B. Saager, D. J. Cuccia, and A. J. Durkin, "Determination of optical properties of turbid media spanning visible and near-infrared regimes via spatially modulated quantitative spectroscopy," *J. Biomed. Opt.* **15**(1), 017012 (2010).
17. W. G. Zijlstra, A. Buursma, and W. P. Meeuwsen-van der Roest, "Absorption spectra of human fetal and adult oxyhemoglobin, de-oxyhemoglobin, carboxyhemoglobin, and methemoglobin," *Clin. Chem.* **37**(9), 1633–1638 (1991).
18. A. K. Dunn et al., "Spatial extent of oxygen metabolism and hemodynamic changes during functional activation of the rat somatosensory cortex," *Neuroimage* **27**(2), 279–290 (2005).
19. H. J. van Staveren et al., "Light scattering in Intralipid-10% in the wavelength range of 400–1100 nm," *Appl. Opt.* **30**(31), 4507–4514 (1991).
20. S. T. Flock et al., "Optical properties of Intralipid: a phantom medium for light propagation studies," *Lasers Surg. Med.* **12**(5), 510–519 (1992).
21. R. Michels, F. Foschum, and A. Kienle, "Optical properties of fat emulsions," *Opt. Express* **16**(8), 5907–5925 (2008).
22. J. R. Mourant et al., "Predictions and measurements of scattering and absorption over broad wavelength ranges in tissue phantoms," *Appl. Opt.* **36**(4), 949–957 (1997).
23. D. J. Weiss, K. J. Wardrop, and O. W. Schalm, *Schalm's Veterinary Hematology*, 6th ed., Wiley-Blackwell, Ames, Iowa (2010).
24. R.B. Saager et al., "Method for depth-resolved quantitation of optical properties in layered media using spatially modulated quantitative spectroscopy," *J. Biomed. Opt.* **16**(7), 077002 (2011).